Journal of Vacuum Science and Technology B

RESEARCH ARTICLE | OCTOBER 13 2023

Identification of dust particles on a periodic nanostructured substrate using scanning electron microscope imaging

EP FREE

Special Collection: Papers from the 66th International Conference on Electron, Ion and Photon Beam Technology and Nanofabrication (EIPBN 2023)

Andrew Tunell; Lauren Micklow; Nichole Scott; Stephen Furst; Chih-Hao Chang

J. Vac. Sci. Technol. B 41, 062804 (2023)
https://doi.org/10.1116/6.0003043

JVST B
Journal of Vacuum Science & Technology B
ARTICLE
pubs.aip.org/avs/jvb

Identification of dust particles on a periodic nanostructured substrate using scanning electron microscope imaging

Cite as: J. Vac. Sci. Technol. B **41**, 062804 (2023); doi: 10.1116/6.0003043
Submitted: 4 August 2023 · Accepted: 19 September 2023 ·
Published Online: 13 October 2023

View Online Export Citation CrossMark

Andrew Tunell,[1] Lauren Micklow,[2] Nichole Scott,[2] Stephen Furst,[2] and Chih-Hao Chang[1,a)]

AFFILIATIONS

[1]Walker Department of Mechanical Engineering, University of Texas at Austin, Austin, Texas 78712
[2]Smart Material Solutions, Inc., Raleigh, North Carolina 27607

Note: This paper is part of the Special Topic Collection: Papers from the 66th International Conference on Electron, Ion and Photon Beam Technology and Nanofabrication (EIPBN 2023).
[a)]**Electronic mail:** chichang@utexas.edu

ABSTRACT

Dust-mitigating surfaces typically consist of high-aspect-ratio structures that separate particles from resting on the bulk material, thereby limiting adhesion due to short-range van der Waals forces. These surfaces can find uses in solar-panel coatings and a variety of dust-resistant optics. The current method for quantifying surface contamination is optical microscopy, but this method is inadequate for observing particles at the submicrometer scale due to the diffraction limit. Furthermore, regardless of the microscopy technique, particle identification becomes problematic as the particle contaminates approach the same length scale of the surface structures. In this work, we demonstrate a method to identify micro-/nanoparticle contaminates on nanostructured surfaces using electron microscopy and image processing. This approach allows the characterization of particles that approach the length scale of the surface structures. Image processing, including spectrum filters and edge detection, is used to remove the periodic features of the surface nanostructure to omit them from the particle counting. The detection of these small particles using electron microscopy leads to an average of 5.62 particles/100 μm^2 detected compared to 0.63 particles/100 μm^2 detected for the traditional confocal optical detection method. Beyond dust-mitigation nanostructures, the demonstrated particle detection technique can find applications in nanobiology, the detection of ice nucleation on a structured surface, and semiconductor mask inspections.

I. INTRODUCTION

Nanostructures are able to create many unique surface properties including dry adhesives, self-cleaning surfaces, and anti-ice materials. Gaining inspiration from the structure of Gecko setae, dry adhesive surfaces can be made from branching high-aspect-ratio nanostructures that conform to the roughness of a surface, maximizing the short-range van der Waals force.[1] In a similar manner, self-cleaning[2] and anti-ice[3,4] surfaces take advantage of the lotus effect.[5] This effect is based on nano-/microscale textures along with low surface energy, which together prevent water from fully wetting the surface, effectively suspending a water droplet on a bed of air in the Cassie–Baxter state.[6–10] One particular application of interest is surfaces with low adhesion energy, which can be used in a variety of applications such as dust-mitigating surfaces, which have already shown significant promise.[11–13] These surfaces are of particular interest to missions to the moon where lunar dust causes significant damage to sensors and equipment, limiting the duration of missions.[14,15] Therefore, dust mitigation is recognized as one of the main obstacles for continued space exploration.[15] In addition, particle contamination causes many problems for terrestrial applications, including in the optics, automobile, aerospace, and healthcare industries.[2,11,12,16–21] For example, solar panels must be frequently cleaned to maintain efficiency that can be reduced by up to 40% if not properly maintained.[11,12,16,19,20]

One challenge in the study of dust-mitigating surfaces is the quantification of the dust-reduction effect. Particle identification is especially difficult when the dust particles are at a similar length scale to the nanoscale to microscale surface features. Another key challenge is characterization throughput that limits whether the technique can be scaled for applications requiring large areas. There are many existing methods to detect particles,[22–28] but all have limiting factors for this use case. Specifically, to detect particles on a nanostructured substrate, the detection approach must be able to discern between the particles and features of the substrate. The system must also be able to characterize relatively large areas in a reasonable time frame. Along with this, the method must retain high enough resolution to resolve individual particles and gather collective data on size. Many methods exist to detect particles moving through fluid by measuring a signal change caused by particles moving through a sensor. Such devices include a resistive pulse sensor coupled with a fluorescent particle detector,[22,23] which together detect particles moving through a channel. Similar methods are used to detect airborne particles including devices, which detect changes in the intensity of a beam of light when particles cross, or a sensor that can detect changes in emitted α-particles such as in a smoke detector.[24,25] These devices are very accurate for detecting relatively high concentrations of particles but are limited by the need for a fluid to carry the particles.

On the other hand, methods for detecting particle contaminates on a flat substrate are relatively limited compared to detection in a fluid. Common methods include optical confocal microscopy and scanning electron microscopy (SEM) inspection. A confocal microscope generates a topographic map of a surface, and thereby, any raised point can be identified as a contaminant. This method is very accurate when detecting defects on a flat surface[26] but is limited in that its accuracy decreases as the surface roughness increases, causing many particles to sit above or below the focal plane. Furthermore, the lateral resolution of an optimized confocal microscope is around 180 nm, but the axial resolution is limited to around 500 nm. This limit in axial resolution prevents the microscope from resolving individual defects and creates challenges when trying to resolve particles in close proximity. SEM inspection methods offer a far higher resolution and depth of field, allowing individual particles to be resolved, even if the surface is not perfectly flat. Recent works have demonstrated precise particle counting on a flat substrate using both SEM imaging and transmission electron microscope (TEM) imaging.[27,28] However, this approach is generally limited to relatively low particle concentrations as the particle detection is done manually by locating the particle edges, thereby limiting the metrology throughput.[27] In studies where particle detection is performed automatically through the software analysis of a TEM image,[28] a high contrast between the particle and a flat substrate is required. Furthermore, the identification of particles on nanostructures with features that have a similar length scale is challenging and less studied.[13] Concurrently, as dust-mitigating structures get more effective against all particles larger than the features, it is critical to identify very small particles that can potentially overcome the antiadhesion effects.

In this work, we present a method for detecting particles on a nanostructured substrate with similar feature sizes using SEM imaging and image processing. This approach employs Fourier filtering to remove periodic nanostructures on the surface and identify dust particles that are smaller than the structures. A multistep particle detection method is used to identify each particle, allowing for large areas to be inspected in a short time frame. The proposed method is experimentally compared with particle identification using confocal microscopy on nanostructured dust-mitigation substrates with 500 nm period. The detection of these small particles using these methods led to an increase of 5.62 particles/100 μm^2 detected, compared to 0.63 particles/100 μm^2 for the traditional confocal optical detection method, successfully demonstrating the detection of particles smaller than features of the periodic nanostructures. This approach improves the metrology of micro/nanoscale particles on nanostructured surfaces and can find applications in quantifying the dust-mitigation performance of these structures as well as identifying and characterizing contaminates in semiconductor and display manufacturing.

II. EXPERIMENT

The fabrication of the dust-mitigating nanostructures in this work is done via a high-throughput nanocoining method using thermal nanoimprint to create periodic structures in polycarbonate substrates.[13,29,30] These structures have a period of 500 nm, an aspect ratio of 0.86, and a tip radius of 150 nm. For this experiment, the samples are coated with a 10 nm thick layer of gold

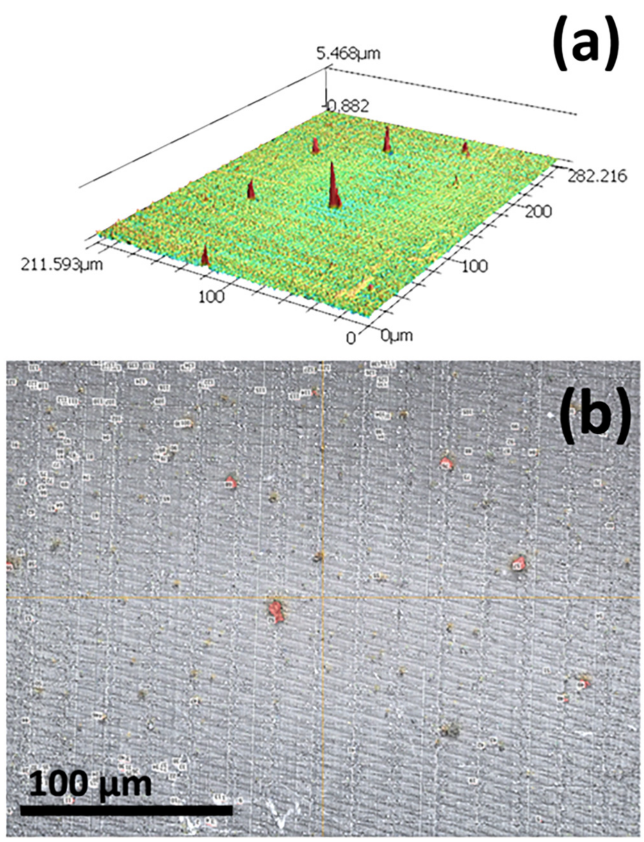

FIG. 1. Representative outputs of the particle-counting method using confocal microscopy. (a) Measured height map of the nanostructured surface with particles after tilt and warp corrections. (b) Resulting image of regions identified as particles are shaded and numbered.

using a sputter coater to reduce charging effects during SEM imaging. Samples without gold sputtering are also fabricated to examine the effects of charging on the particle-identification algorithm. The patterned surfaces are then chemically treated to reduce their surface energy. This is accomplished by cleaning the substrates with oxygen plasma etching to activate the surface hydroxyl groups and coating a monolayer of trichloro(octyl)silane using vapor phase deposition. After surface treatment, the static contact angle of the 500 nm periodic nanostructure increased from 111.7° to 132.9°, demonstrating a decrease in the surface energy. The prepared samples are then contaminated by spooning on a thick layer of lunar dust (Exolith, LMS-1; lunar mare simulant)[31] to completely cover the surface. The covered samples are then tilted vertically to allow the dust to be removed via gravity. The remaining dust contaminates on the samples are inspected using both confocal microscopy (Keyence VK-X1100 Confocal Microscope) and SEM.

For baseline comparison, confocal microscopy analysis was conducted to generate a topographic map of the surface. The file analyzer included with the microscope software is used to identify particles in each obtained image using the following procedure. First, any tilt of the surface is removed by creating a reference plane through the manual selection of dust-free areas in each of the four corners in the image. Since the substrate is a flexible polycarbonate, any warping of the surface is removed by fitting the surface to a higher-order polynomial. The resulting image then shows all parts of the bare nanostructured surface at approximately the same height as shown in Fig. 1(a). Once this is visually verified, any raised points on the surface can be identified by setting a height threshold and minimum area, as shown in Fig. 1(b). The threshold parameters are typically set manually in a case-by-case basis depending on the effectiveness of the reference-plane and waveform-removal procedures. In this analysis, the height threshold is set to 300 nm and the minimum area is set to 550 nm, slightly larger than the nanostructure features so that the surfaces structures will not be counted as particles. The program then outputs the area and diameter of the identified particle regions, allowing the particle coverage area to be calculated as the percentage of the surface that is covered by residual particles. This method works well for large dust particles since they tend to rest on the tips of the nanostructures and are easily identified. On the other hand, particles close to the length scale of the nanostructures are often missed. Reducing the threshold parameters to count the smaller particle would result in large areas of the nanostructured surface to be counted as well, resulting in an overestimate of the particle coverage area.

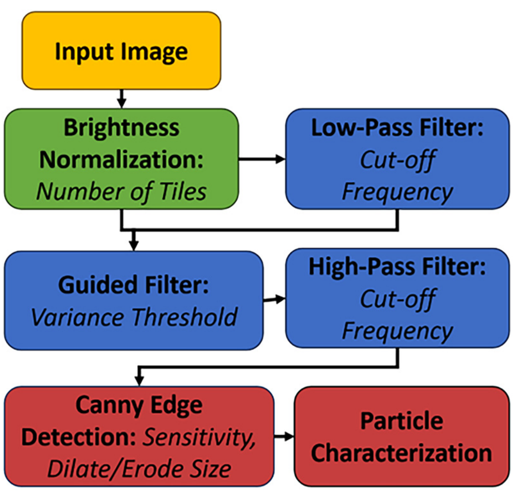

FIG. 2. Block diagram of image filtering and particle detection algorithm with the key parameters for each step.

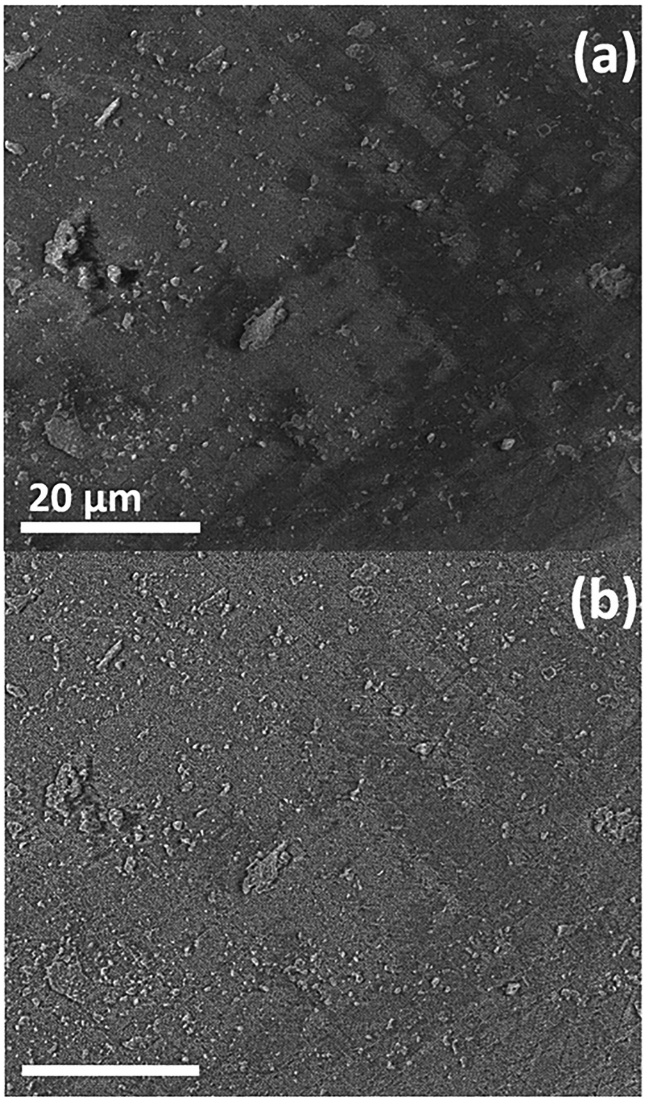

FIG. 3. Top-view SEM images of a particle-contaminated sample without gold coating before (a) and after (b) brightness normalization using adaptive histogram equalization.

The particle detection method used in this study is based on SEM imaging and image processing. The SEM offers many advantages due to its higher resolution, which allows small particles to be resolved even if they rest below the nanostructures. Two significant challenges occur when using the SEM identification method. First, it is difficult to identify the particles due to poor contrast between the nanostructures and the particles, which yield the same secondary electron signals during imaging. Second, the high resolution of the SEM causes the individual features of the periodic nanostructures to be identified by traditional particle-counting programs causing significant overestimates in the particle coverage area.

For this work, a custom algorithm was implemented in MATLAB to overcome these challenges. The algorithm includes multiple image filtering techniques as well as a multiple-stepped approach to identify the particles, as illustrated in Fig. 2. The first operation performed by the program is to normalize the brightness and contrast in the obtained SEM due to nonuniform electron signals. This step is especially necessary for nongold coated samples where charging effects cause regions to have a wide range of signal brightness. Normalization is performed using adaptive histogram equalization that divides up the image into a set number of tiles, generates a histogram of the brightness values in

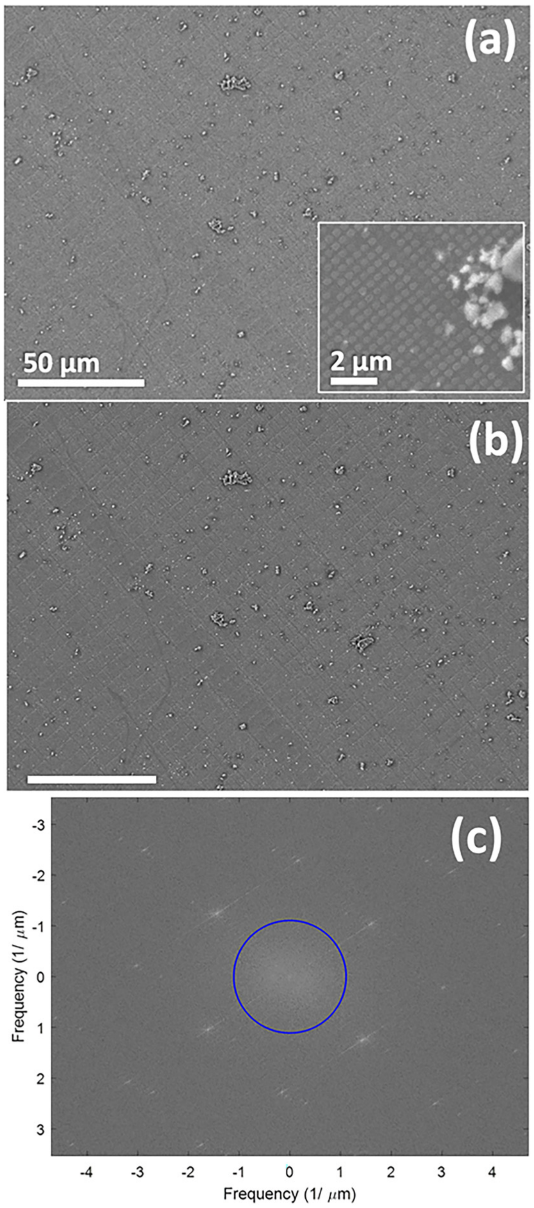

FIG. 4. Low-pass filtering process using Fourier transform. (a) Normalized-brightness image to be filtered using adaptive histogram equalization. The inset image depicts a separate higher magnification micrograph showing the nanostructured surface. (b) Resulting image after high-frequency signals have been filtered. (c) Fourier transform of the normalized image with an overlayed low-pass filter.

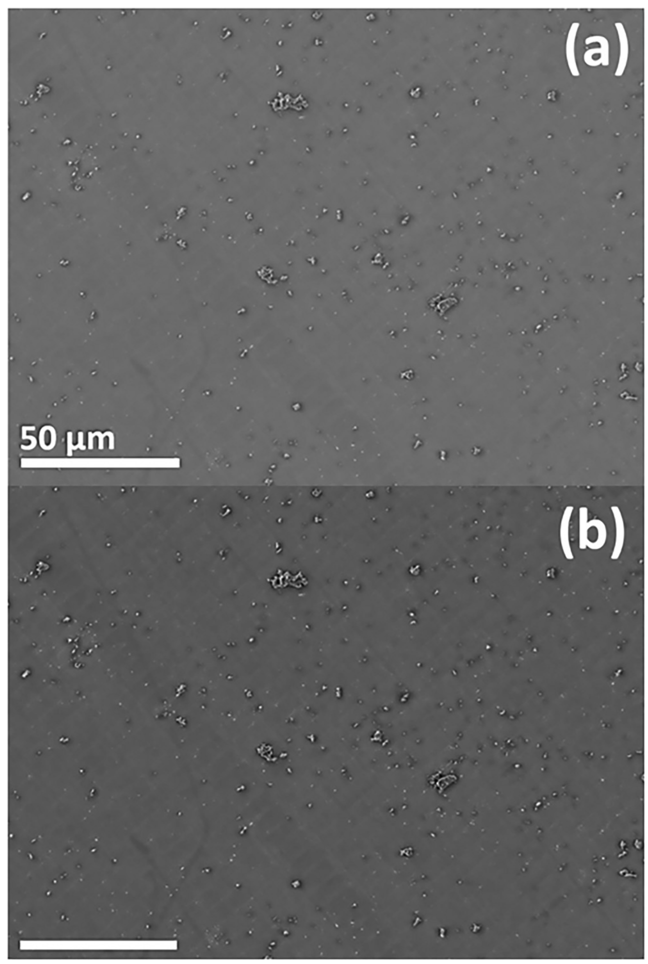

FIG. 5. Effects of the guided filter. (a) The guided-filtered image and (b) the high-pass filter applied to guided-filtered image.

each tile, and then adjusts the histogram to fit the desired distribution. In our case, the images are divided into 16 384 tiles (128×128 divisions) and the brightness histogram was fit to a Rayleigh distribution. An example of the output of this process for a bare polycarbonate sample with 500 nm nanostructures is shown in Fig. 3.

After brightness and contrast normalization, the 2D Fourier transformation of the image is calculated using fast Fourier transform (FFT) to analyze the spatial-frequency spectra. An example of this process is shown in Fig. 4, wherein the starting image is of a sample that was gold coated and the dimensions of the image are identical to what is obtained from the confocal microscope for comparison. The distinct peaks of the periodic nanostructures can be clearly observed in Fig. 4(c), which is aligned at around 45° and shows a fourfold symmetry for the square lattice. The fundamental frequency can be identified as $f_o = 2\,\mu\text{m}^{-1}$, corresponding to the $\Lambda = 1/f_o = 500\,\text{nm}$ period structures fabricated. Higher-order harmonics can also be observed. The high-frequency signals are then removed using a low-pass filter that effectively removes the periodic elements from the image. To set the cut-off frequency of the image, the radius of the depicted blue circle can be adjusted and any frequencies outside of this circle will be removed. For this work, a cut-off frequency of $0.9 f_o$ is selected to filter out the first- and higher-order peaks while preserving as much of the components near DC. The filtered image and its corresponding frequency spectra are shown in Figs. 4(b) and 4(c), respectively, which shows the effective removal of the periodic surface structures.

Next, the images are smoothed using gaussian filtering to remove artifacts induced from the previous steps while still retaining the details of the dust particles. To do this, a guided filter is used where the Fourier-filtered image acts as the guide and the brightness normalized image is filtered. The function selectively applies a mean filter everywhere except where edges are detected in the guide image, allowing details of the dust particles to be recovered while further blurring the background nanostructure as shown in Fig. 5(a). The variance threshold parameter referenced in Fig. 2 modifies the allowable brightness variance in a given radius before it will identify as an edge. Therefore, a higher variance threshold causes increased smoothing of edges.[32] After these steps, the surface nanostructures appear to be adequately removed. To further enhance the boundaries of the dust particle contaminates, a high-pass filter with a cut-off frequency of $0.1 f_o$ is used to increase the edge contrast. The filtered image is shown in Fig. 5(b), which has sharpened particle edges and can improve the accuracy of the edge-detection algorithm.

The edges of the particles are then identified using the Canny method,[33] as illustrated in Fig. 6. This method accurately selected many of the particle edges but due to the rough surfaces of the dust

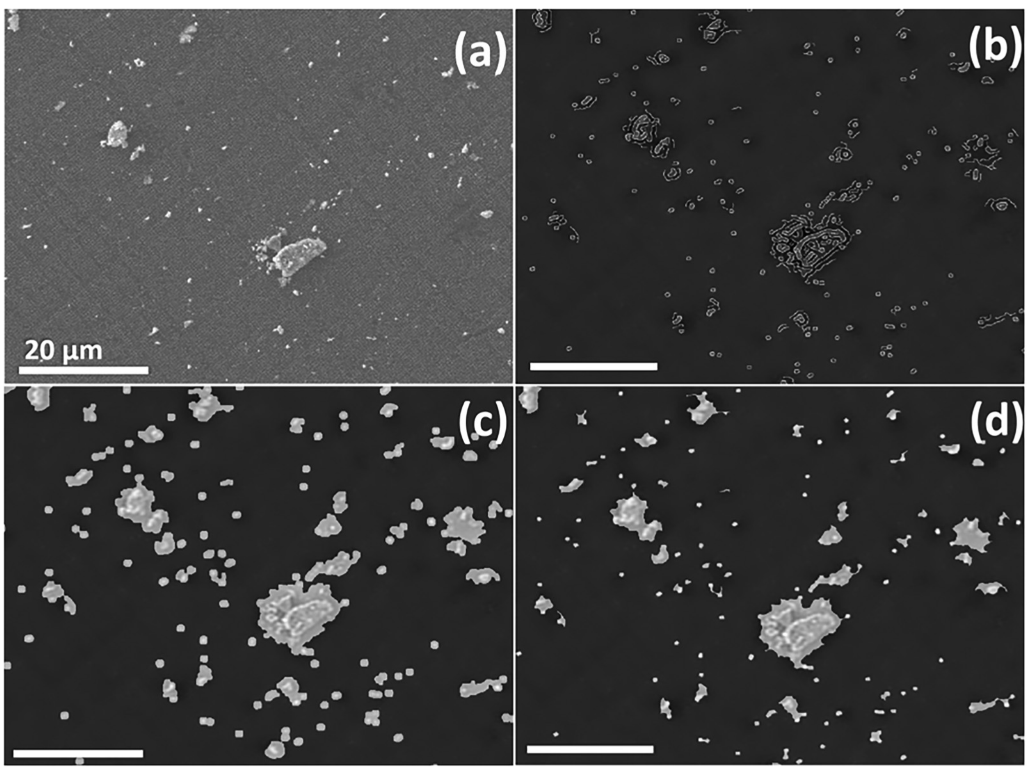

FIG. 6. Illustrated results using the Canny edge-detection algorithm. (a) The original unfiltered SEM image and corresponding (b) base edge detection and (c) dilated edge detection. (d) Particles identified after edges were eroded by the same dilation amount.

TABLE I. Experimentally obtained averaged values from all confocal and SEM analyses.

Measurement type	Average diameter (μm)	Coverage area (%)	Particles/ 100 μm^2
Confocal, gold coated	1.77	0.52	0.238
SEM, gold coated	1.28	3.48	2.547
Confocal, no gold	2.44	5.00	1.030
SEM, no gold	2.21	19.07	8.701

particles, many edges are detected on the interiors. These interior lines cause the fill function to not cover the entire particle, as lines drawn within the particles form closed loops that are not filled, leading to hollow particles that are not physical. This is best demonstrated in Fig. 6(b), showing the result from the unmodified edge-detection method. To get the particles to be completely enclosed, the as drawn edges are expanded using the dilate function, which expands the width of the drawn edges by a set number of pixels. This caused the interior lines within a particle to connect, and the small gaps that are not already covered can be closed using a fill function. This filling operation introduces one more challenge in that the particle coverage areas are slightly overestimated as shown in Fig. 6(c). To correct for this, a final step was performed to cut back slightly on the drawn edges using the erode function that cuts around the as drawn edges using a structuring element with a set radius in pixels.[34,35] This command removes all filled areas without overlapping the originally drawn edges using a structuring element.

Finally, once the particles are all detected and filled, a simple command is used to label each particle with a number. The tabulated data on each particle area and diameter are generated in micrometer units. These data can then be used to directly compare with the particle coverage area and average particle diameter values obtained from the confocal particle-identification method. The particle identified using both confocal and SEM methods was verified manually to ensure that the counting has been performed correctly.

III. RESULTS AND DISCUSSION

The SEM particle-counting program demonstrated excellent results in most cases but also revealed some persisting problems. For this work, images are taken with an FEI Quanta 650 ESEM using a beam energy of 10 kV and a resolution of 3072×1920. A variety of SEM images were analyzed by the program with inspection areas ranging from 1000to 60 000 μm^2 as well as images of gold-coated samples and nongold-coated samples. The program worked best for gold-coated samples with low particle density and minimal particle grouping but was still able to identify particles under worst-case conditions albeit with lower accuracy. In addressing the characterization throughput, the estimated time to analyze 100 images is calculated for each method. These values are estimated by averaging the processing, equipment, and setup time it has taken for collecting the images in this study and previous studies. To capture and analyze 100 images, it is estimated that the confocal method would take about 370 min, whereas the SEM is estimated to take only 170 min. The time saving for the image analysis step is even higher, where the processing per image of the confocal takes on average 2 min, whereas the SEM particle-counting program takes less than 10 s per image after configuration. Therefore, the proposed SEM approach would only take 20 min to

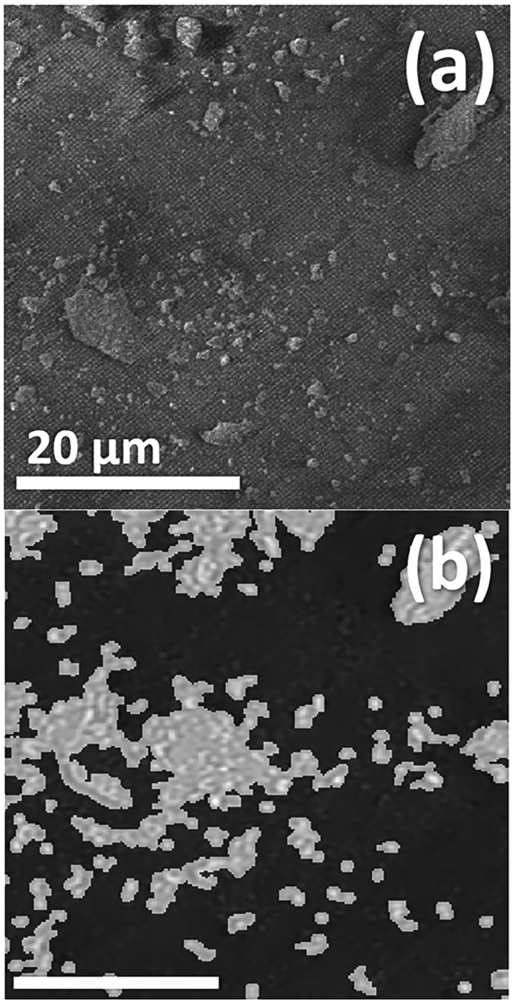

FIG. 7. Illustration of worst-case scenario of low contrast and particle grouping artifact. (a) Original SEM image of the nongold-coated sample and (b) initial particle detection with particle grouping artifact.

process 100 images, whereas the confocal method would require 170 min.

For the SEM image that covered the exact same dimensions as the confocal image ($282 \times 211\ \mu m^2$), the surface area coverage was determined to be $2.87 \pm 0.96\%$, whereas the confocal analysis gave a coverage of $0.52 \pm 0.20\%$. From the ten confocal images collected, an average of 142.4 particles was detected in the 59 500 μm^2 inspection area. However, the SEM analysis detected 824 particles in the same inspection area. To confirm that the SEM was effectively detecting smaller particles, the average particle diameters are also calculated. For the SEM, the average particle diameter is $1.27 \pm 0.52\ \mu m$, whereas the confocal reported an average diameter of $1.78 \pm 0.1\ \mu m$. These error bars were determined by taking the standard deviation of the reported averages based on seven SEM images and five confocal Images. These results clearly demonstrate that the added resolution of SEM imaging allows for the improved detection of small particles. In fact, in every test performed spanning both gold and nongold coated samples as well as the range of inspection areas, the SEM particle detection method yielded a higher number of particles counted. The count of particles with the SEM method was also manually confirmed by overlaying each region the program identified as a particle on the original image to verify that there is a particle corresponding to each area.

To directly compare the confocal and SEM methods, the number of particles per $100\ \mu m^2$ area is calculated. For the nongold-coated samples, the measured particle densities are 1.03 and 8.70 particles/100 μm^2 for confocal and SEM, respectively. It should be noted that for the gold-coated samples, fewer particles are observed for both detection methods as the gold coating decreases the adhesion force by removing the contribution from static charge. For this case, the measured particle densities are 0.24 and 2.55 particles/$100\ \mu m^2$ for confocal and SEM, respectively. A summary of these data comparing both the gold-coated and bare polycarbonate samples for both detection methods is shown in Table I; these data include the averages of all magnifications looked at. The average diameter measurement is the average value of all particles identified on the sample, which is an important parameter for determining which size of particles the structure is effective against. The coverage area is used to determine how effective the antidust structures are by examining what percentage of the surface retained residual dust. Finally, the number of particles detected within a 100 μm^2 area is a good reference figure for the ability of the measurement devices to resolve the dust particles.

While the proposed approach allows more accurate detection of particles, it also faces challenges for smaller particles. One unavoidable problem with the SEM particle detection program is separating large groups of particles. The dilation method used to fully fill in each particle also resulted in nearby particles being connected. This problem is especially evident for the nongold-coated samples where charging from the SEM creates low contrast between the particles and the substrate. This effect is demonstrated in Fig. 7(b), where a large group of scattered particles are grouped together as one large particle. In this worst-case scenario of very low contrast along with grouped particles, significant errors are

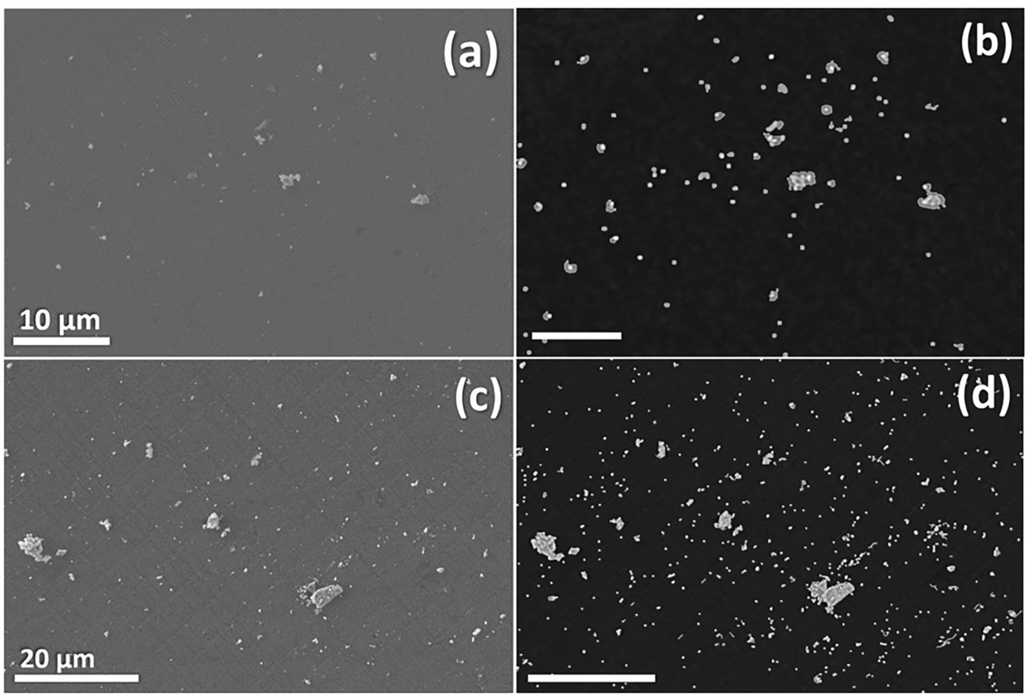

FIG. 8. Demonstration of particle counting for various inspection areas of gold-coated samples. 3500 μm^2 area showing (a) original SEM and (b) identified particles. 13 000 μm^2 area showing (c) original SEM and (d) identified particles.

made in the program by overcounting the actual area covered. It should be noted that images with higher contrast, including all the gold-coated samples, are not subjected widely to this problem. Furthermore, even including the grouping effect, which counts closely clustered particles as a single particle, the average particle diameters are still smaller than the confocal measurements.

For the gold-coated samples, the SEM images are much sharper and exhibit little charging. In examining the particle detection of these samples, the program appeared to detect each particle very accurately at a wide range of magnifications. Figure 8 shows the detection of particles at higher magnifications with inspection areas of 3500 (a) and 13 000 μm^2 (b). These images gave average particle diameters of 1.18 and 1.17 μm and a particle coverage area of 1.52% and 3.38% for the higher and lower magnifications, respectively. The higher particle coverage for the higher magnification images can be attributed to operator bias since large particles can cover the majority of the field of view at this scale and, therefore, are omitted during SEM imaging. In addition, while the higher magnification images can better resolve smaller particles, the corresponding areas are smaller. A higher magnification allows for increased resolution to identify smaller particles but also creates higher variation in the particle area coverage as a smaller region of the sample is inspected. The lowest magnification analysis is demonstrated earlier when comparing the analysis to the same inspection area as the confocal.

In future work, we will examine the size distributions of detected particles on the nanostructured surfaces. Improvements for detecting particles on the nongold coated samples will also be made so that the samples can be reused after inspection. As it stands, the current method of particle detection for these samples does work well for relative comparisons as the grouping of particles is consistent for all samples. Furthermore, the dilation process that allows particles to be fully detected also increases the area that is counted for each particle; this results in an artificial increase in the particle coverage area. The degree of area estimation will be examined further by using higher magnification SEM images, which is a part of on-going research. A major benefit of the SEM particle detection over the confocal analysis is the removal of bias from the user. The confocal program requires a manual input for the height threshold at which the particles to be counted and provides visual feedback as this value is changed. In contrast, the SEM particle analysis only requires a manual input when selecting the low-pass filter size, a parameter that is coupled to the feature size of the nanostructured surface and does not directly change the number of particles counted. In this way, the SEM particle detection becomes more repeatable and avoids unconscious skewing of the data. For this reason, even with the existing problems, specifically, the overestimation of the particle coverage area due to particle grouping and dilation, the SEM particle detection method performs better for quantifying the degree of residual dust particles on a nanostructured surface. Future work will focus on implementing automatic SEM imaging over large areas to calculate the particle distribution across the entire substrates.

IV. SUMMARY AND CONCLUSIONS

This research demonstrates a more accurate and repeatable method for quantifying the degree of dust particle contamination on a periodic nanostructure. The proposed method of quantifying dust contamination uses SEM imaging to resolve features smaller than possible with traditional optical methods. In addition, Fourier filters prevent any periodic elements of the underlying substrate from being counted as particles. In the experiment, the proposed method showed an increase in detected particle densities from 0.24 and 2.55 particles/100 μm^2 for confocal and SEM, respectively. This result demonstrates significant improvement in the detection of dust particles on a periodic nanostructure, allowing for the improved quantification of dust-mitigating properties. However, these results are best used for relative comparisons as problems with overcounting due to feature dilation as well as grouping persist but are constant among equally magnified images. In addition, the proposed SEM detection method can be tuned for a wide range of applications that involve the detection of defects on a periodic structure. This can include the inspection of semiconductor masks, detection of particles in nanobiology, and detection of nucleation sites on a structured surface.

ACKNOWLEDGMENTS

This work was performed at UT Austin Texas Materials Institute (TMI), the Nanomanufacturing System for mobile Computing and Energy Technologies (NASCENT), and Texas Nanofabrication Facilities, which was supported by the National Science Foundation (NSF) as part of the National Nanotechnology Coordinated Infrastructure (NNCI) Grant (No. NNCI-2025227). This work was supported by the National Aeronautics and Space Administration (NASA) under Grant No. 80NSSC21C0252.

AUTHOR DECLARATIONS

Conflict of Interest

The authors have no conflicts to disclose.

Author Contributions

Andrew Tunell: Formal analysis (equal); Investigation (equal); Writing – original draft (equal). **Lauren Micklow:** Writing – review & editing (supporting). **Nichole Scott:** Writing – review & editing (supporting). **Stephen Furst:** Writing – review & editing (supporting). **Chih-Hao Chang:** Writing – review & editing (equal).

DATA AVAILABILITY

The data that support the findings of this study are available within the article.

REFERENCES

[1]K. Autumn *et al.*, Proc. Natl. Acad. Sci. U. S. A. **99**, 12252 (2002).
[2]K.-C. Park, H. J. Choi, C.-H. Chang, R. E. Cohen, G. H. McKinley, and G. Barbastathis, ACS Nano **6**, 3789 (2012).
[3]C. Wang, T. Fuller, W. Zhang, and K. J. Wynne, Langmuir **30**, 12819 (2014).
[4]L. Mishchenko, B. Hatton, V. Bahadur, J. A. Taylor, T. Krupenkin, and J. Aizenberg, ACS Nano **4**, 7699 (2010).
[5]K.-C. Chang *et al.*, ACS Appl. Mater. Interfaces **5**, 1460 (2013).
[6]L. Gao and T. J. McCarthy, Langmuir **22**, 6234 (2006).

[7]A. Dove, G. Devaud, X. Wang, M. Crowder, A. Lawitzke, and C. Haley, Planet. Space Sci. **59**, 1784 (2011).
[8]R. Fürstner, W. Barthlott, C. Neinhuis, and P. Walzel, Langmuir **21**, 956 (2005).
[9]B. Bhushan, Y. C. Jung, and K. Koch, Langmuir **25**, 3240 (2009).
[10]S. Aramrak, M. Flury, and J. B. Harsh, Langmuir **27**, 9985 (2011).
[11]N. Cherupurakal, M. Mozumder, A. Mourad, and S. Lalwani, Renewable Sustainable Energy Rev. **151**, 111538 (2021).
[12]R. Isaifan, D. Johnson, L. Ackermann, B. Figgis, and M. Ayoub, Sol. Energy Mater. Sol. Cells **191**, 413 (2019).
[13]S. S. Lee, L. Micklow, A. Tunell, K.-C. Chien, S. Mohanty, N. Cates, S. Furst, and C.-H. Chang, ACS Appl. Mater. Interfaces **15**, 13678 (2023).
[14]L. Taylor, H. Schmitt, W. Carrier, and M. Nakagawa, in *1st Space Exploration Conference: Continuing the Voyage of Discovery* (AIAA, 2005), p. 2510.
[15]N. Afshar-Mohajer, C.-Y. Wu, J. S. Curtis, and J. R. Gaier, Adv. Space Res. **56**, 1222 (2015).
[16]J. Zhu, C.-M. Hsu, Z. Yu, S. Fan, and Y. Cui, Nano Lett. **10**, 1979 (2010).
[17]D. Sun and K. F. Böhringer, Microsyst. Nanoeng. **6**, 1 (2020).
[18]D. Goossens, Sol. Energy **163**, 131 (2018).
[19]A. Sayyah, M. N. Horenstein, and M. K. Mazumder, Sol. Energy **107**, 576 (2014).
[20]S. Ghazi, A. Sayigh, and K. Ip, Renewable Sustainable Energy Rev. **33**, 742 (2014).
[21]M. G. Khalfallah and A. M. Koliub, Desalination **209**, 209 (2007).
[22]X. Wu, C. H. Chon, Y.-N. Wang, Y. Kang, and D. Li, Lab Chip **8**, 1943 (2008).
[23]D. Holmes, H. Morgan, and N. G. Green, Biosens. Bioelectron. **21**, 1621 (2006).
[24]R. Tian, C. Dierk, C. Myers, and E. Paulos, in *Proceedings of the 2016 CHI Conference on Human Factors in Computing Systems*, San Jose, CA, 7–12 May 2016 (Association for Computing Machinery, New York, 2016), pp. 1338–1348.
[25]E. G. Bakhoum, IEEE Sens. J. **12**, 3031 (2012).
[26]A. R. Stivers *et al.*, in *22nd Annual BACUS Symposium on Photomask Technology*, Monterey, CA, 30 September–4 October 2002 (SPIE, Bellingham, WA, 2002), pp. 408–417.
[27]H. Bresch, V.-D. Hodoroaba, A. Schmidt, K. Rasmussen, and H. Rauscher, Nanomaterials **12**, 2238 (2022).
[28]E. Verleysen, T. Wagner, H.-G. Lipinski, R. Kägi, R. Koeber, A. Boix-Sanfeliu, P.-J. De Temmerman, and J. Mast, Materials **12**, 2274 (2019).
[29]N. Cates, V. J. Einck, L. Micklow, J. Morère, U. Okoroanyanwu, J. J. Watkins, and S. Furst, Nanotechnology **32**, 155301 (2021).
[30]E. Zdanowicz, T. A. Dow, and R. O. Scattergood, Nanotechnology **23**, 415303 (2012).
[31]"Lunar mare (LMS-1) high-fidelity moon dirt simulant," Exolith Lab, https://exolithsimulants.com/products/lms-1-lunar-mare-simulant (accessed May 5, 2022).
[32]K. He, J. Sun, and X. Tang, IEEE Trans. Pattern Anal. Mach. Intell. **35**, 1397 (2013).
[33]J. Canny, IEEE Trans. Pattern Anal. Mach. Intell. **PAMI-8**, 679 (1986).
[34]R. Van Den Boomgaard and R. Van Balen, CVGIP Graph. Models Image Process. **54**, 252 (1992).
[35]R. C. Gonzales, R. E. Woods, and S. L. Eddins, *Digital Image Processing Using MATLAB*, 3rd ed. (Gatesmark Publishing, Knoxville, TN, 2020)).